FULL PAPER

Nickel pivalate complexes: structural variations and magnetic susceptibility and inelastic neutron scattering studies

Grégory Chaboussant*†[a] Reto Basler,[a] Hans-Ulrich Güdel,*[a] Stefan Ochsenbein,[a] Andrew Parkin,[c] Simon Parsons,[c] Gopalan Rajaraman,[b] Andreas Sieber,[a] Andrew A. Smith,[b] Grigore A. Timco[d] and Richard E. P. Winpenny*[b]

[a] *Department of Chemistry and Biochemistry, University of Bern, Freiestrasse 3, CH-3000 Bern 9, Switzerland*

[b] *Department of Chemistry, The University of Manchester, Oxford Road, Manchester, UK M13 9PL*

[c] *Department of Chemistry, The University of Edinburgh, West Mains Road, Edinburgh, UK EH9 3JJ*

[d] *Institute of Chemistry, Moldova Academy of Sciences, Academei Str. 3, Kishinev, Moldova MD-2028*

The synthesis and structural characterisation of three small nickel(II) cages are reported, all stabilised by pivalate ligands. The magnetic properties of the cages have been studied by a combination of susceptibility measurements and inelastic neutron scattering. For a dinuclear cage, $[Ni_2(\mu\text{-}OH_2)(O_2CCMe_3)_4(HO_2CCMe_3)_4]$ **1** the ground state is $S = 2$, with a ferromagnetic exchange interaction between the Ni(II) centres of $J = 0.32$ meV and $D_{S=2} = -0.09$ meV in the ground state. For a tetranuclear heterocubane cage, $[Ni_4(\mu_3\text{-}OMe)_4(O_2CCMe_3)_4(MeOH)_4]$ **2**, two ferromagnetic exchange interactions are found and an $S = 4$ ground state observed. While the zero-field splitting of this state cannot be determined unambigiously the most likely value is $D_{S=4} = -0.035$ meV. For a tetranuclear nickel butterfly, $[Ni_4(\mu_3\text{-}OH)_2(O_2CCMe_3)_6(EtOH)_6]$ **3**, three exchange interactions are required, two anti-ferromagnetic and one weakly ferromagnetic; the resulting ground state is $S = 0$. The data enable us to estimate the zero-field splitting of single Ni(II) ions involved in the cage as $D_i = +1.0$ meV. Both **1** and **2** are therefore expected to be new single molecule magnets.

Introduction

The enormous increase in the attention paid to magnetic clusters has been mainly due to the discovery that molecular species can show slow relaxation of magnetisation under certain circumstances.[1] This phenomena, known as "single molecule magnetism", is exciting because it suggests it could be possible to store magnetic information in a single molecule rather than in much larger magnetic particles. The unusual quantum phenomena[2] the molecules display have also led some to propose the molecules could be used as Qbits in quantum computers.[3]

The behaviour occurs because the spin ground state of these molecules, S, is high and the anisotropy of this state is large and of the "easy-axis" type. This is best measured by the magnitude of the axial zero-field splitting parameter D, which for a single molecule magnet (SMM) has to be negative. The energy barrier to reorientation of the magnetisation is then given by:

$$E_a = |D|S^2$$

for integer spins and

$$E_a = |D|(S^2 - 1/4)$$

for half-integer spins.

Therefore to make technologically useful SMMs, this barrier needs to be as large as possible. Before this is possible we need to understand how the parameters D and S vary from structure to structure. A difficulty arises because the traditional method of studying magnetic properties, magnetic susceptibility measurements at variable temperature, do not produce unambiguous results for complexes where both S and D are large. At least two SMMs had erroneous spin ground states assigned when the initial magnetic

measurements were made. Therefore methods beyond magnetic studies are necessary if our understanding of such molecules is to be improved. Magnetic inelastic neutron scattering (INS) is a powerful technique to determine exchange couplings and single-ion anisotropy in molecular magnets.[4] Here we report studies of some simple nickel complexes that use inelastic neutron scattering to derive spin Hamiltonian parameters directly; these values are consistent with magnetic susceptibility measurements.

Experimental

Preparation of compounds

All reagents, metal salts and ligands were used as obtained from Aldrich. Analytical data were obtained by the microanalytical service of the Universities of Edinburgh and Manchester.

All manipulations in the synthesis of compounds **2** and **3** were carried out under a nitrogen atmosphere. **2** and **3** are not sufficiently stable to allow IR spectra to be recorded.

$[Ni_2(\mu\text{-}OH_2)(O_2CCMe_3)_4(HO_2CCMe_3)_4]$ **1.** This compound can be obtained by several methods: two of them are described here.

Method A. Nickel carbonate hydroxide tetrahydrate (3.0 g, 5.1 mmol) was reacted with an excess of pivalic acid (15 g, 150 mmol) at 160 °C for 3 h, leading to dissolution of the carbonate salt. The yellow-green solution was cooled to room temperature, and Et₂O (30 ml) was added and the mixture stirred briefly. The solution was filtered and the Et₂O evaporated by heating up to 70 °C. MeCN (50 ml) was added with stirring and cooled to room temperature in an open flask, which allows absorption of H₂O from air. Green crystals of **1** suitable for X ray analysis form in one day. At this point a few drops of H₂O (0.2–0.3 ml) were added to the solution, leading to a green solution and **1** crystallises spontaneously. **1** was collected by filtration, washed with cold MeCN and dried in a slow flow of N₂. **1** has a high solubility at room temperature in a wide range of

† Present address: Laboratoire Léon Brillouin, CNRS-CEA, CEA Saclay, 91191 Gif-sur-Yvette, France.

Table 1 Experimental data for the X-ray studies of **1–3**

Compound	**1**	**2**	**3**
Formula	$C_{40}H_{78}Ni_2O_{17}$	$C_{28}H_{64}Ni_4O_{16}.\ 4.5CH_4O$	$C_{44}H_{90}Ni_4O_{20}.\ 2C_2H_6O$
M	948.4	1035.8	1242.1
Crystal system	Orthorhombic	Orthorhombic	Monoclinic
Space group	$Pbca$	$Pbca$	$P2_1/n$
a/Å	12.024(3)	15.929(2)	12.708(2)
b/Å	19.102(5)	15.433(2)	13.924(3)
c/Å	47.828(12)	42.067(7)	18.590(6)
β/°	90	90	91.87(2)
U/Å^3	10986(5)	10341(3)	3287.8(15)
T/K	150(2)	150(2)	220(2)
Z	8	8	2^b
D_c/g cm^{-3}	1.147	1.331	1.255
μ/mm^{-1}	0.743	2.185	1.192
Unique data	11210	9096	5818
Unique data with $F_o > 4\sigma F_o$)	8076	6448	3397
Parameters/restraints	540/676	532/30	334/2
$R1$, $wR2^a$	0.0613, 0.1818	0.0615, 0.1737	0.0631, 0.1700

^{a} $R1$ based on observed data, $wR2$ on all unique data. ^{b} The molecule lies on an inversion centre.

organic solvents (from MeCN to pentane) giving a green solution. It is soluble also in H_2O. Yield 10.5 g (86.7%). Found, %: C, 50.91; H, 8.35; N, 0.0; Ni, 12.23. Calc. for $C_{40}H_{78}Ni_2O_{17}$, C, 50.66; H, 8.29; N, 0.0; Ni, 12.38. IR (KBr, v/cm^{-1}): 2974 (s), 1677 (vs), 1602 (vs), 1577 (m), 1547 (w), 1482 (s), 1460 (m), 1407 (s), 1362 (s), 1327 (s), 1211 (vs), 1078 (w), 1032 (w), 938 (w), 899 (m), 876 (m), 799 (m), 772 (m).

Method B. Nickel hydroxide (3.0 g, 32 mmol) and pivalic acid (15 g, 150 mmol) were refluxed in toluene (50 ml) for 3 h with stirring. The green solution formed after dissolution of nickel hydroxide was filtered using a blue band quality filter and the solvent was evaporated in air at room temperature with occasional stirring until the volume was *ca.* 10ml. Green crystals of **1** suitable for X ray analysis form during this time. MeCN (25 ml) was added to increase the amount of **1** that crystallised. The solid was collected by filtration, washed with cold acetonitrile and dried in N_2. Yield 10.5 g (68.4%). Found, %: C, 50.89; H, 8.24; N, 0.0; Ni, 12.27. Calc. for $C_{40}H_{78}Ni_2O_{17}$, C, 50.66; H, 8.29; N, 0.0; Ni, 12.38.

[Ni$_4$(μ_3-OMe)$_4$(O$_2$CCMe$_3$)$_4$(MeOH)$_4$] 4 MeOH 2. **1** (3.0 g, 3.2 mmol) was heated in a flow of N_2 at 200 °C for 3.5 h. The green compound decomposes to give a yellow-brown powder; this was collected and dissolved in MeOH (20.0 ml) at 60 °C. The solution was cooled to room temperature and green crystals of **2** formed which were collected by filtration after 2 days and washed with cold MeOH. Yield: 0.65g, 40.3%. Found: C, 36.91; H, 7.81. Calc. for $C_{32}H_{80}Ni_4O_{20}$ C, 37.69, H, 7.91.

[Ni$_4$(μ_3-OH)$_2$(O$_2$CCMe$_3$)$_6$(EtOH)$_6$]. 2EtOH 3. **1** (3.0 g, 3.16 mmol) was heated in a flow of N_2 at 200 °C for 3.5 h. The green compound decomposes to give a yellow-brown powder which was dissolved in EtOH (60.0 ml) at 80 °C. The solution was cooled to room temperature and green crystals of **3** were formed, which were collected by filtration after 2 days and washed with cold EtOH. Yield: 0.73g, 37.1%. Found: C, 44.34; H, 8.82, Ni, 18.24. Calc. for $C_{46}H_{104}Ni_4O_{22}$ C, 44.41, H, 8.43, Ni, 18.87

Crystallography

Crystal data and data collection and refinement parameters for compounds **1–3** are given in Table 1, selected bond lengths and angles in Tables 2–4.

Data collection and processing

Data were collected with a Bruker Smart APEX CCD area detector equipped with an Oxford Cryosystems low-temperature device,[5] using Mo–Ka radiation: ω scans for **1** and **2**; ω–2ϕ scans for **3**. Data were corrected for Lorentz and polarisation factors. Absorption corrections were applied to all data.

Table 2 Selected bond lengths (in Å) and angles (in °) for **1**

Ni(1)–O(1B)	2.018(3)	Ni(2)–O(2A)	2.019(3)
Ni(1)–O(1A)	2.031(2)	Ni(2)–O(2B)	2.033(3)
Ni(1)–O(12)	2.033(2)	Ni(2)–O(12)	2.040(2)
Ni(1)–O(1E)	2.054(2)	Ni(2)–O(1F)	2.052(3)
Ni(1)–O(1D)	2.072(3)	Ni(2)–O(1H)	2.068(3)
Ni(1)–O(1C)	2.078(3)	Ni(2)–O(1G)	2.082(3)
O(1B)–Ni(1)–O(1A)	93.05(11)	O(2A)–Ni(2)–O(2B)	92.76(11)
O(1B)–Ni(1)–O(12)	98.02(11)	O(2A)–Ni(2)–O(12)	98.34(11)
O(1A)–Ni(1)–O(12)	91.98(10)	O(2B)–Ni(2)–O(12)	91.76(10)
O(1B)–Ni(1)–O(1E)	88.99(11)	O(2A)–Ni(2)–O(1F)	89.64(12)
O(1A)–Ni(1)–O(1E)	175.43(11)	O(2B)–Ni(2)–O(1F)	175.42(11)
O(12)–Ni(1)–O(1E)	91.79(10)	O(12)–Ni(2)–O(1F)	91.75(10)
O(1B)–Ni(1)–O(1D)	86.60(12)	O(2A)–Ni(2)–O(1H)	86.87(12)
O(1A)–Ni(1)–O(1D)	85.96(11)	O(2B)–Ni(2)–O(1H)	85.70(11)
O(12)–Ni(1)–O(1D)	175.05(11)	O(12)–Ni(2)–O(1H)	174.31(11)
O(1E)–Ni(1)–O(1D)	90.07(10)	O(1F)–Ni(2)–O(1H)	90.54(11)
O(1B)–Ni(1)–O(1C)	172.37(11)	O(2A)–Ni(2)–O(1G)	173.70(11)
O(1A)–Ni(1)–O(1C)	89.39(11)	O(2B)–Ni(2)–O(1G)	89.21(11)
O(12)–Ni(1)–O(1C)	89.11(10)	O(12)–Ni(2)–O(1G)	87.58(10)
O(1E)–Ni(1)–O(1C)	88.08(10)	O(1F)–Ni(2)–O(1G)	88.00(11)
O(1D)–Ni(1)–O(1C)	86.37(11)	O(1H)–Ni(2)–O(1G)	87.30(12)
Ni(1)–O(12)–Ni(2)	111.24(11)		

Structure analysis and refinement

Structures **1** and **3** were solved by heavy atom methods using DIRDIF;[6] structure **2** was solved by direct methods using SHELXS-97. All structures were completed by iterative cycles of ΔF-syntheses and full-matrix least-squares refinement. All non-H atoms were refined anisotropically in all structures. In all structures difference Fourier syntheses were employed in positioning idealised methyl-hydrogen atoms which were assigned isotropic thermal parameters [U(H) = $1.5U_{eq}$(C)], and allowed to ride on their parent C-atoms [C–H 0.93 Å].

Some or all of the pivalate groups in each structure show rotational disorder. Details of the disorder, and modelling strategies used are given in the supplementary material. All refinements were against F^2 and used SHELXL-97.[7]

CCDC reference numbers 236895–236897.

See http://www.rsc.org/suppdata/dt/b4/b406112h/ for crystallographic data in .cif or other electronic format.

INS experimental details

The experiments were carried out on the time-of-flight (TOF) spectrometers FOCUS at the SINQ neutron source (PSI, Switzerland) and IN6 at the ILL (Grenoble, France).

Polycrystalline samples of typically 1–3 g placed under helium in thin rectangular aluminium slabs (30 × 50 mm) of 1 to 3 mm thickness were used. The slabs were inserted in an ILL orange cryostat. Data were taken at temperatures between 1.5K and 40K.

Table 3 Selected bond lengths (in Å) and angles (in °) for **2**

Ni(1)–O(1B)	2.024(3)	Ni(3)–O(1D)	2.026(3)
Ni(1)–O(124)	2.037(3)	Ni(3)–O(123)	2.044(3)
Ni(1)–O(123)	2.045(3)	Ni(3)–O(234)	2.056(3)
Ni(1)–O(134)	2.057(3)	Ni(3)–O(134)	2.057(3)
Ni(1)–O(1A)	2.121(3)	Ni(3)–O(31)	2.082(3)
Ni(1)–O(2A)	2.138(3)	Ni(3)–O(32)	2.096(3)
Ni(2)–O(2B)	2.009(3)	Ni(4)–O(2D)	2.020(3)
Ni(2)–O(234)	2.037(3)	Ni(4)–O(124)	2.042(3)
Ni(2)–O(124)	2.054(3)	Ni(4)–O(134)	2.048(3)
Ni(2)–O(123)	2.060(3)	Ni(4)–O(41)	2.060(3)
Ni(2)–O(1C)	2.118(3)	Ni(4)–O(234)	2.066(3)
Ni(2)–O(2C)	2.155(3)	Ni(4)–O(42)	2.101(3)
Ni(1)–Ni(2)	2.8384(11)	Ni(3)–Ni(4)	2.9070(11)
O(1B)–Ni(1)–O(124)	94.06(13)	O(1D)–Ni(3)–O(123)	170.05(13)
O(1B)–Ni(1)–O(123)	93.33(13)	O(1D)–Ni(3)–O(234)	91.85(12)
O(124)–Ni(1)–O(123)	89.42(11)	O(123)–Ni(3)–O(234)	80.03(12)
O(1B)–Ni(1)–O(134)	170.97(12)	O(1D)–Ni(3)–O(134)	93.94(12)
O(124)–Ni(1)–O(134)	79.94(12)	O(123)–Ni(3)–O(134)	79.98(12)
O(123)–Ni(1)–O(134)	79.95(12)	O(234)–Ni(3)–O(134)	86.86(12)
O(1B)–Ni(1)–O(1A)	89.92(13)	O(1D)–Ni(3)–O(31)	90.60(13)
O(124)–Ni(1)–O(1A)	166.57(13)	O(123)–Ni(3)–O(31)	95.67(13)
O(123)–Ni(1)–O(1A)	103.17(12)	O(234)–Ni(3)–O(31)	94.08(13)
O(134)–Ni(1)–O(1A)	97.45(12)	O(134)–Ni(3)–O(31)	175.33(13)
O(1B)–Ni(1)–O(2A)	90.29(13)	O(1D)–Ni(3)–O(32)	91.38(13)
O(124)–Ni(1)–O(2A)	105.53(12)	O(123)–Ni(3)–O(32)	96.85(13)
O(123)–Ni(1)–O(2A)	164.34(13)	O(234)–Ni(3)–O(32)	176.64(13)
O(134)–Ni(1)–O(2A)	97.79(13)	O(134)–Ni(3)–O(32)	93.84(13)
O(1A)–Ni(1)–O(2A)	61.57(12)	O(31)–Ni(3)–O(32)	84.97(15)
O(2B)–Ni(2)–O(234)	171.62(12)	O(2D)–Ni(4)–O(124)	170.13(12)
O(2B)–Ni(2)–O(124)	93.92(13)	O(2D)–Ni(4)–O(134)	94.16(12)
O(234)–Ni(2)–O(124)	80.23(12)	O(124)–Ni(4)–O(134)	80.01(12)
O(2B)–Ni(2)–O(123)	93.83(13)	O(2D)–Ni(4)–O(41)	90.40(14)
O(234)–Ni(2)–O(123)	80.11(12)	O(124)–Ni(4)–O(41)	95.44(13)
O(124)–Ni(2)–O(123)	88.55(11)	O(134)–Ni(4)–O(41)	175.43(14)
O(2B)–Ni(2)–O(1C)	89.30(13)	O(2D)–Ni(4)–O(234)	91.97(12)
O(234)–Ni(2)–O(1C)	97.64(12)	O(124)–Ni(4)–O(234)	79.82(12)
O(124)–Ni(2)–O(1C)	168.16(12)	O(134)–Ni(4)–O(234)	86.81(12)
O(123)–Ni(2)–O(1C)	102.62(12)	O(41)–Ni(4)–O(234)	92.78(13)
O(2B)–Ni(2)–O(2C)	90.20(12)	O(2D)–Ni(4)–O(42)	90.71(13)
O(234)–Ni(2)–O(2C)	97.25(12)	O(124)–Ni(4)–O(42)	97.55(13)
O(124)–Ni(2)–O(2C)	107.34(12)	O(134)–Ni(4)–O(42)	93.44(13)
O(123)–Ni(2)–O(2C)	163.31(12)	O(41)–Ni(4)–O(42)	86.76(14)
O(1C)–Ni(2)–O(2C)	61.20(12)	O(234)–Ni(4)–O(42)	177.28(13)
Ni(3)–O(123)–Ni(1)	100.44(13)	Ni(4)–O(134)–Ni(1)	99.60(13)
Ni(3)–O(123)–Ni(2)	99.76(13)	Ni(4)–O(134)–Ni(3)	90.17(11)
Ni(1)–O(123)–Ni(2)	87.49(12)	Ni(1)–O(134)–Ni(3)	99.63(13)
Ni(1)–O(124)–Ni(4)	100.45(13)	Ni(2)–O(234)–Ni(3)	100.10(13)
Ni(1)–O(124)–Ni(2)	87.85(11)	Ni(2)–O(234)–Ni(4)	99.85(13)
Ni(4)–O(124)–Ni(2)	100.09(13)	Ni(3)–O(234)–Ni(4)	89.67(11)

Table 4 Selected bond lengths (in Å) and angles (in °) for **3**. Symmetry transformations used to generate equivalent atoms: #1 −x, −y, −z + 1

Ni(1)–O(1B)	1.998(4)	Ni(2)–O(2B)	2.018(4)
Ni(1)–O(1)	2.005(4)	Ni(2)–O(1)	2.034(4)
Ni(1)–O(1C)	2.060(4)	Ni(2)–O(2C)	2.046(4)
Ni(1)–O(11)	2.095(4)	Ni(2)–O(13)	2.075(4)
Ni(1)–O(1A)	2.119(4)	Ni(2)–O(1)#1	2.085(4)
Ni(1)–O(2A)	2.163(4)	Ni(2)–O(12)	2.119(4)
O(1B)–Ni(1)–O(1)	102.05(16)	O(2B)–Ni(2)–O(1)	98.46(17)
O(1B)–Ni(1)–O(1C)	92.86(19)	O(2B)–Ni(2)–O(2C)	90.18(18)
O(1)–Ni(1)–O(1C)	92.46(16)	O(1)–Ni(2)–O(2C)	98.27(16)
O(1B)–Ni(1)–O(11)	91.41(19)	O(2B)–Ni(2)–O(13)	89.29(19)
O(1)–Ni(1)–O(11)	90.76(16)	O(1)–Ni(2)–O(13)	169.75(16)
O(1C)–Ni(1)–O(11)	174.00(17)	O(2C)–Ni(2)–O(13)	88.35(19)
O(1B)–Ni(1)–O(1A)	160.80(17)	O(2B)–Ni(2)–O(1)#1	177.70(16)
O(1)–Ni(1)–O(1A)	97.14(16)	O(1)–Ni(2)–O(1)#1	82.69(15)
O(1C)–Ni(1)–O(1A)	86.93(18)	O(2C)–Ni(2)–O(1)#1	91.62(16)
O(11)–Ni(1)–O(1A)	87.66(18)	O(13)–Ni(2)–O(1)#1	89.34(17)
O(1B)–Ni(1)–O(2A)	99.78(17)	O(2B)–Ni(2)–O(12)	87.74(18)
O(1)–Ni(1)–O(2A)	158.09(16)	O(1)–Ni(2)–O(12)	87.31(15)
O(1C)–Ni(1)–O(2A)	88.34(16)	O(2C)–Ni(2)–O(12)	174.28(16)
O(11)–Ni(1)–O(2A)	86.79(17)	O(13)–Ni(2)–O(12)	86.30(18)
O(1A)–Ni(1)–O(2A)	61.03(16)	O(1)#1–Ni(2)–O(12)	90.33(15)
Ni(1)–O(1)–Ni(2)	110.46(17)	Ni(2)–O(1)–Ni(2)#1	97.31(15)
Ni(1)–O(1)–Ni(2)#1	128.92(18)		

The incoming neutron wavelength λ was selected according to the energy range under interest. The angle between the incoming beam and the surface of the sample holder was 135° to insure an optimised scattering towards the ³He detector banks. On FOCUS and IN6, the

scattering angle 2θ covers the range from $+10°$ to $+130°$ and $+10°$ to $+114°$, respectively.

Data treatment involved the subtraction of a spectrum of an empty aluminium container of the same size and the calibration of the detectors by means of a spectrum of vanadium metal. The time-of-flight to energy conversion and the data reduction were done using the programs INX (ILL) an NINX (PSI).

Approximately 3 g (3 mm thickness) of deuterated **1** was studied using a neutron wavelength of $\lambda = 5$ Å (FOCUS) and 5.9 Å (IN6). The experimental energy resolution defined as the full width at half-maximum (FHWM) at the elastic position was FWHM ≈ 0.1 meV (FOCUS) and 0.05 meV (IN6). Approximately 0.5 g (1 mm thickness) of deuterated **2** and 1.5 g (1 mm thickness) of **3** were studied using a neutron wavelength of $\lambda = 3.1$ Å with an experimental energy resolution at the elastic position of FWHM ≈ 0.3 meV. Importantly, the experimental widths observed at inelastic positions are systematically larger than the elastic resolution as a consequence of the TOF technique (elastic focusing mode).

Due to the size of the samples and to the amount of incoherent scattering in these materials, long counting times were necessary to obtain reasonable statistics (10 h). In addition, large chunks of detectors were grouped together to increase statistics. This is justified by the fact that only moderate change of the inelastic scattering intensity could be observed as a function of scattering angle 2θ. However, in some instances, it was possible to track the Q-dependence of the INS peaks through the study of the intensity variation as a function of 2θ.

Magnetic measurements

Finally, susceptibility measurements on powder samples were carried out between 1.8 K and 300 K using a 5 T Quantum Design MPMS-XL SQUID magnetometer with applied magnetic fields between 100 G and 1000 G. Sample sizes of typically 40–50 mg were used (**1**: 46.3 mg, **2**: 40.6 mg, **3**: 48.3 mg)

Results

Synthesis and structures

The starting point for this chemistry is the dinuclear complex $[Ni_2(\mu\text{-}OH)_2(O_2CCMe_3)_4(HO_2CCMe_3)_4]$ **1** (Fig. 1). **1** is made by direct reaction of basic nickel carbonate or nickel hydroxide with pivalic acid, followed by crystallisation by adding MeCN. The two nickel(II) sites are bridged by two 1,3-bridging carboxylates and by an oxygen atom, which we assign as a μ-water molecule. Compounds containing this core $\{Ni_2(H_2O)(O_2CR)_2\}$ have been reported previously (see below). The coordination sphere at each six coordinate Ni site is completed by two protonated pivalate ligands, and by one deprotonated pivalate. The deprotonated pivalates form strong H-bonds (2.56 and 2.51 Å) to the μ-OH$_2$. This raises a question of whether the more accurate description is as a μ-OH$_2$ and two deprotonated pivalates or as a μ-O and two HO$_2$CCMe$_3$ ligands.

Heating **1** to 180 °C leads to an ill-defined highly hygroscopic yellow–brown compound, **A**. **A** has an unusually low solubility in non-polar solvents for complexes of pivalate. Thermogravimetric analysis show that up to 220 °C **1** lost 45% of its weight, which suggests loss of all neutral ligands. This leads us to suggest **A** is probably polymeric with the formula $[Ni(O_2CCMe_3)_2]_n$. **A** is extremely reactive, dissolving and reacting with a range of alcohols. In MeOH a tetranuclear heterocubane, $[Ni_4(\mu_3\text{-}OMe)_4(O_2CCMe_3)_4(MeOH)_4]$ **2**, forms with methoxide supplying the O-atoms at the alternate sites of the heterocubane (Fig. 2). Two pivalates chelate to each of Ni(1) and Ni(2). Two further pivalates act as 1,3-bridges between Ni(1) and Ni(2), and Ni(3) and Ni(4) respectively. The remaining coordination sites on Ni(3) and Ni(4) are occupied by four MeOH ligands.

There are two distinct nickel sites in **2**. Two involve chelating pivalates while two are each bound to two terminal solvates. The reaction of **A** with other alcohols also produces tetranuclear cages where there are two distinct nickel sites (Fig. 3). However in EtOH
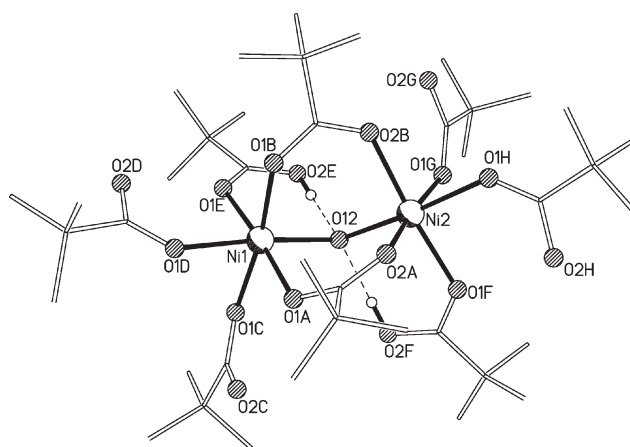

Fig. 1 The structure of **1** in the crystal. C-atoms shown as lines and H-atoms omitted for clarity except for H-atoms involved in hydrogen bonding. H-bonds shown as dashed lines.
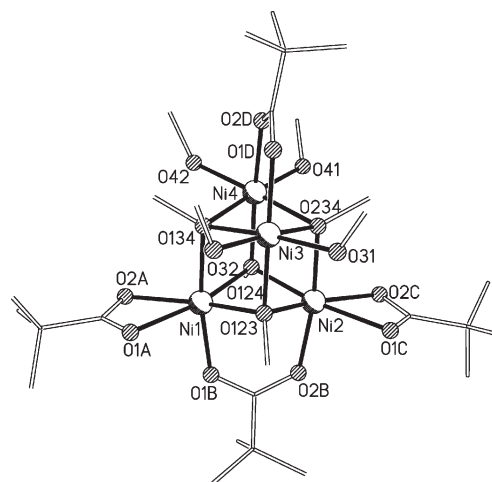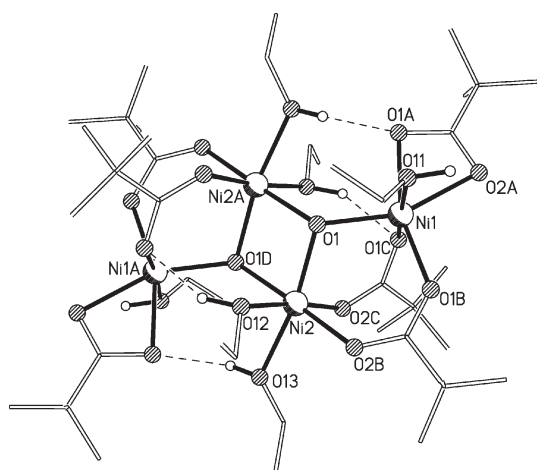

Fig. 2 The structure of **2** in the crystal. C-atoms shown as lines and H-atoms omitted for clarity.

the differences between the sites are more pronounced than in **1**. $[Ni_4(\mu_3\text{-}OH)_2(O_2CCMe_3)_6(EtOH)_6]$ **3**, which has crystallographic inversion symmetry, contains a butterfly of nickel (II) sites, with the "body" of the butterfly [Ni(2) and Ni(2a)] bridged by two μ_3-hydroxides; these OH groups also bridge to Ni "wing-tip" sites [Ni(1) and Ni(1a)]. Two of the edges of the butterfly are also bridged by two 1,3-pivalates, while the two alternating edges have no bridge beyond the μ_3-OH. All the metal sites are six-coordinate, with the coordination sphere at the wing-tip sites completed by a chelating pivalate and one EtOH molecule, while at the body sites the coordination is completed by two EtOH molecules. The structure of **3** can be regarded as a dimerisation of **1**, with the "dinuclear" fragment comprising one body and one wing-tip nickel bridged by a μ-OH and two pivalates which has dimerised through the hydroxide group binding to a second dinuclear block. The equivalent cluster can be made from ^{n}PrOH

The difference in reactivity that leads to **2** and **3** is presumably related to the ease of deprotonated of MeOH and EtOH. While methoxide is found in **2**, no alkoxides are found in **3**. Therefore the more protic solvent is leading to a heterocubane, while the less acidic solvent retains the proton and merely coordinates in vacant sites on the periphery of the cage. A similar trend in reactivity is found in analogous cobalt pivalate chemistry.

Magnetic measurements and inelastic neutron scattering studies

Fig. 4 shows the static susceptibility of **1** represented as χT versus T, measured at $H = 100$ G. At temperatures above *ca.* 150K, the χT product reaches a constant value of about 2.57 emu K mol^{-1}. As the temperature is lowered below 150K, χT rapidly increases, goes

Fig. 3 The structure of **3** in the crystal. C-atoms shown as lines and H-atoms omitted for clarity except for H-atoms involved in hydrogen bonding. H-bonds shown as dashed lines.
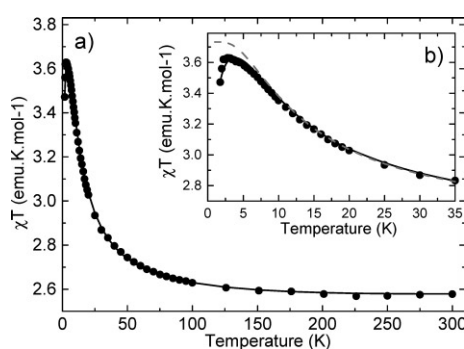

Fig. 4 DC-SQUID susceptibility, χ, of **1** represented as χT versus T between 1.5 K and 300 K under an applied external field of 100 G. (a) Full temperature scale. (b) Close-up look at the low temperature region. Solid line represents best fit[23] with $g = 2.23$, $J = 0.32$ meV and $D_0 = -0.09$ meV. Dashed line is a calculated curve with $g = 2.23$, $J = 0.32$ meV and $D_0 = 0$.
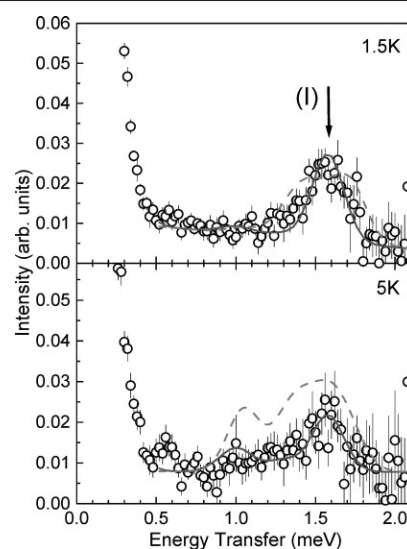

Fig. 5 INS spectra of a powdered sample of **1** obtained at 1.5 K and 5 K on the spectrometer FOCUS (PSI) with $\lambda = 5.0$ Å (incident energy $E_i = 3.272$ meV). All the detectors were grouped together to optimise signal-to-noise ratio. In this configuration, the scattering vector Q is integrated between $Q_{min} = 0.5$ Å^{-1} and $Q_{max} = 2.0$ Å^{-1}. The small peak at 0.55 meV is an experimental artefact. INS simulation as discussed in the text are shown as lines with $J = 0.32$ meV and $D_0 = +0.09$ meV (dashed line) or $D_0 = -0.09$ meV (solid line). For each case, only one overall scaling factor has been used for both temperatures.
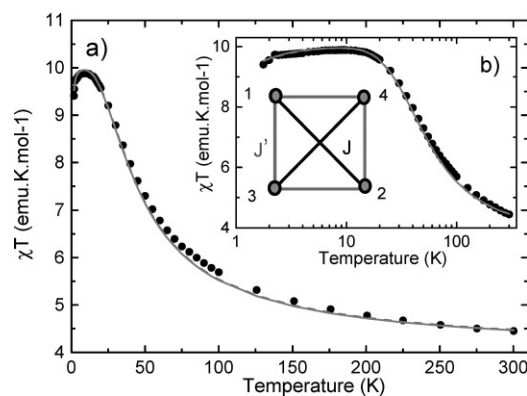

Fig. 6 DC-SQUID susceptibility, χ, of **2** represented as χT versus T between 1.5K and 300K under an applied external field of 100 G. (a) Full temperature scale. (b) temperature in logarithmic scale. Solid lines represent equally best fits[23] with $J = 1.047$ meV, $J' = 0.56$ meV, $g = 2.0$ and $D_i = +0.38$ meV or $D_i = -0.27$ meV. Inset: Schematic representation of the magnetic exchange scheme in **2**.

through a maximum at about 2.6 K and then sharply decreases upon further cooling. The paramagnetic limit is consistent with two spins $S = 1$ and $g = 2.26$ as expected for a Ni(II) dimer. The low temperature increase is characteristic of a ferromagnetic (FM) coupling between the two magnetic centres. The maximum value for χT at 2.6 K is consistent with an $S = 2$ cluster ground state and $g = 2.20$. The sharp low temperature downturn is attributed to the effect of single-ion anisotropy as discussed later.

The powder inelastic neutron scattering (INS) spectrum of **1**, measured on FOCUS with $\lambda = 5.0$ Å is shown in Fig. 5 at two different temperatures (1.5 K and 5 K). The elastic line has a full width at half-maximum (FWHM) of about 0.1 meV. Only one inelastic peak, at $\hbar\omega_1 = 1.57$ meV, could be observed in the available energy window. Its intensity is slightly decreasing with increasing temperature and the Q-dependence of the intensity has a maximum between 1 Å^{-1} and 1.5 Å^{-1}. These two observations strongly suggest that the peak is due to magnetic transition(s). This peak will be labelled (I) hereafter. We also notice a small broadening or shift towards low energies as the temperature is increased. A spectrum obtained on IN6 (ILL) at a higher wavelength ($\lambda = 5.9$ Å) shows that, at lower energies, a small peak (II) appears on the wing of the elastic line at an energy around $\hbar\omega_2 = 0.27$ meV (not shown). Due to the weak intensity and the large elastic signal underneath it was not possible to extract reliable information concerning its intensity as a function of temperature or scattering vector Q. The anomalous peak at 0.55 meV in Fig. 5 is an experimental artefact specific to this wavelength as no such peak could be observed with $\lambda = 4.5$ Å on FOCUS or $\lambda = 5.9$ Å on IN6.

Fig. 6 shows the static susceptibility of **2** represented as χT versus T, measured at $H = 100$ G. At high temperatures, the χT product reaches progressively a constant value of about 4.66 emu K mol^{-1}. As the temperature is lowered below 100 K, χT rapidly increases and go through a maximum at about 9.5 K and then decreases

upon further cooling down to 1.8 K. The paramagnetic limit at high temperature is consistent with four spins $S = 1$ and $g = 2.16$, consistent with a Ni(II) tetranuclear cluster. The low temperature increase is characteristic of ferromagnetic coupling between the four magnetic centres. The maximum value for χT at 9.5 K is consistent with a $S = 4$ cluster ground state. The sharp downturn below 3 K is attributed to the effect of anisotropy.

The powder inelastic neutron scattering (INS) spectrum of **2**, measured on FOCUS with $\lambda = 3.1$ Å is shown in Fig. 7 at two different temperatures (1.5 K and 40 K). The elastic line has a FWHM of about 0.3 meV. Two weak inelastic peaks can be observed with energies $\hbar\omega_1 = 4.75$ meV and $\hbar\omega_2 = 6.70$ meV. A linear background subtraction of the 1.5 K data is also shown to emphasize the relative intensity of these two peaks. Again, as in **1**, both the temperature- and Q-dependence of the peak intensities are consistent with magnetic scattering. The large incoherent background underneath the magnetic peaks is shown to increase strongly as Q is increased, a definitive sign of phonon scattering.

Fig. 8 shows the static susceptibility χ of **3** as a function of temperature, measured at 1000 G. In the paramagnetic regime, the χT product tends to saturate at about 4.82 emu K mol^{-1} (see inset). This is consistent with four Ni(II) centres with $S = 1$ and $g = 2.19$.

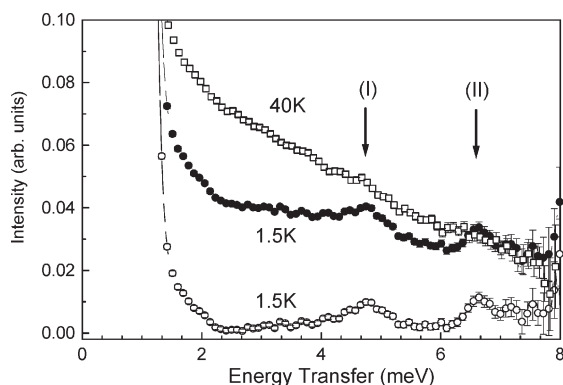**Fig. 7** INS spectra of a powdered sample of **2** obtained at 1.5 K and 40 K on the spectrometer FOCUS (PSI) with $\lambda = 3.1$ Å (incident energy $E_i = 8.51$ meV). All the detectors were grouped together to optimise signal-to-noise ratio. In this configuration, the scattering vector Q is integrated between $Q_{min} = 1.0$ Å^{-1} and $Q_{max} = 3.0$ Å^{-1}. Open circles show the 1.5K data after a linear background subtraction. Arrows indicate the two magnetic transitions $\hbar\omega_1 = 4.75$ meV and $\hbar\omega_2 = 6.70$ meV.
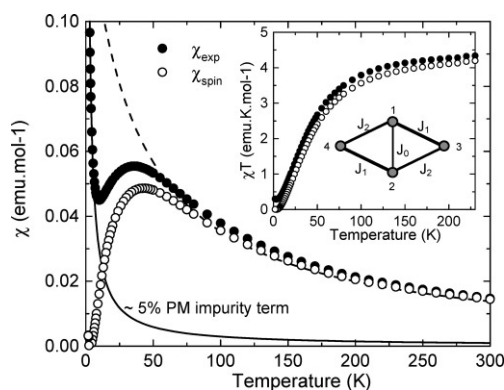
Fig. 8 DC-SQUID susceptibility, χ, (solid circles) of **3** between 1.5K and 300K under an applied external field of 1000G. The inset shows χ represented as χT versus T. A contribution for a 5% paramagnetic impurity (solid line) has been subtracted. The cluster susceptibility $\chi_{spin} = \chi_{exp} - \chi_{imp}$ is shown as open circles. The dashed line represents a Curie–Weiss fit to the high-temperature region with $\theta_{CW} \approx -34$K and a Curie constant of 4.82 emu K mol^{-1}. Inset: Schematic representation of the magnetic exchange scheme in **3**.

As the temperature is lowered, χ first increases, passes through a maximum at about 35 K then goes down before a sharp increase due to a ~5% paramagnetic impurity. The impurity contribution ($\sim 1/T$) can be easily subtracted and the cluster's susceptibility, χ_{spin}, readily goes down to zero at low temperature as shown in Fig. 8. The overall behaviour is characteristic of a system with an $S = 0$ ground state and relatively strong antiferromagnetic (AFM) interactions within the cluster.

The powder INS spectrum of **3**, measured on FOCUS with $\lambda = 3.1$ Å is shown in Fig. 9 at 1.5 K after background subtraction that accounts for incoherent scattering and time-of-flight corrections at high energy transfers. As for **2**, the elastic line has a FWHM of about 0.3 meV. This time, at least three inelastic peaks can be observed with energies $\hbar\omega_1 = 2.8$ meV, $\hbar\omega_3 = 4.5$ meV and $\hbar\omega_4 = 5.6$ meV. There is also a weaker and broad feature at $\hbar\omega_2 = 3.5$–4.0 meV. The Q-dependence of the intensity of the lowest energy peak is consistent with magnetic scattering. At higher energies, the background increases and no clear trend could be discerned.

Discussion

Structural considerations

The structures are not unusual for nickel(II). There are several previous examples of dinuclear nickel(II) cages bridged as **1**. The majority have terminal N-donors as well as O-donors. For example, Turpeinen[8] has reported a series of compounds of formula [Ni$_2$(H$_2$O)(μ-O$_2$CR)$_2$(O$_2$CR)$_2$(tmen)$_2$], where tmen = N,N,N',N'-tetramethyldiaminoethane and R = Me, CH$_2$Cl, Et, CF$_3$, CHCl$_2$,
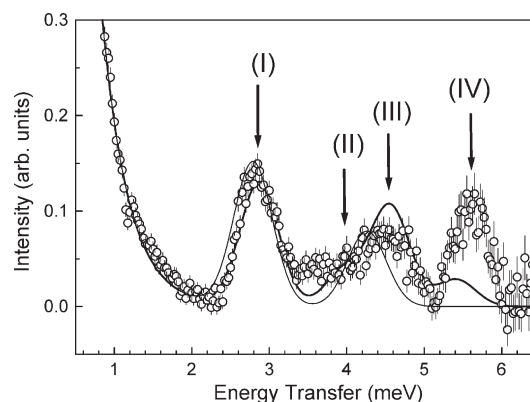
Fig. 9 INS spectra of a powdered sample of **3** obtained at 1.5K on the spectrometer FOCUS (PSI) with $\lambda = 3.1$ Å (incident energy $E_i = 8.51$ meV). The lowest angle detectors were grouped together and, thus, the scattering vector Q is integrated between $Q_{min} = 0.5$ Å^{-1} and $Q_{max} = 1.5$ Å^{-1}. Solid lines are spectrum obtained with single-ion anisotropy (thick solid line) and without (thin solid line) as discussed in the text.

CHMeCl, CH$_2$CH$_2$Cl. Other terminal N-donors used have included pyridine,[9] imidazole,[10] N,N',N''-trimethyl-1,4,7-triazacyclononane[11] and 2,2'-bipyridyl.[12] A series of structures featuring pivalate as the carboxylate with various terminal ligands has been reported by the Eremenko group.[12,13]

Many {Ni$_4$O$_4$} cubanes similar to **2** have also been reported previously, several with μ_3-methoxide providing the four oxygen centres. The first example of which we are aware involves terminal salicylaldehyde and ethanol ligands.[14] Since that date terminal ligands attached to this core have included: acetylacetonate,[15] dibenzoylmethane (dbm),[16,17] 2,4-pentanedionate[18] and 6-chloro-2-pyridonate.[19] Christou and co-workers used magnetic studies on the complex [Ni(μ_3-OMe)(dbm)(MeOH)]$_4$ to derive a correlation between the magnetic exchange between Ni centres and the Ni$\cdots$O$\cdots$Ni angle.[16]

While this paper was in preparation, which has taken some time, Eremenko and co-workers have reported several {Ni$_4$(μ-OH)$_2$} butterflies,[20] including a compound with the same formula as **3**, but with a subtly different unit cell. The other variants reported have alternative terminal ligands to EtOH, e.g. aniline, N-phenyl-1,2-diaminobenzene. Pavlishchuck et al have very recently reported[21] a series of nickel butterflies featuring oximate ligands in place of carboxylates, and with terminal 1,5-diamino-3-azapentane ligands.

Magnetic and spectroscopic behaviour

The magnetic behaviour of the cages is the chief point of interest. In particular, we were interested to examine how well we could model the magnetic data using exchange interactions derived from inelastic neutron scattering, rather than by fitting magnetic data by conventional means. This would be a good demonstration that INS data is a more direct measurement of exchange couplings than the usual procedure of fitting susceptibility data. If we are using more than one method for measuring J, this makes fitting for other spin Hamiltonian parameters more reliable. Combining susceptibility data and INS data reduces the possibility of using a model that is over-parameterised. The results are encouraging.

[Ni$_2$(μ-OH$_2$)(O$_2$CCMe$_3$)$_4$(HO$_2$CCMe$_3$)$_4$] 1

The two Ni(II) $S = 1$ centres in **1** are coupled ferromagnetically as shown by the continuous rise of χT below 100K (Fig. 4). The $S = 1$ state of Ni(II) may be split by second-order spin–orbit coupling in zero field[22] inducing single-ion anisotropy and a zero-field splitting of the ground state. Assuming predominant axial anisotropy, and neglecting dipolar interactions, the appropriate effective spin Hamiltonian at zero magnetic field is given by:

$$H_{Ni_2} = -2J\boldsymbol{S}_1\cdot\boldsymbol{S}_2 + \boldsymbol{S}_1\cdot\boldsymbol{D}_1\cdot\boldsymbol{S}_1 + \boldsymbol{S}_2\cdot\boldsymbol{D}_2\cdot\boldsymbol{S}_2 \qquad (1)$$

where J is the exchange coupling between the two $S = 1$ spins. $\boldsymbol{D}_1$ and $\boldsymbol{D}_2$ are the single-ion anisotropy parameters for each centre.

Considering the symmetry of the dinuclear molecule, we make the reasonable assumption that $\boldsymbol{D}_1 = \boldsymbol{D}_2$. In this case, the Hamiltonian can be written as:

$$H_{Ni_2} = -2J\boldsymbol{S}_1 \cdot \boldsymbol{S}_2 + \boldsymbol{S} \cdot \boldsymbol{D}_S \cdot \boldsymbol{S} \qquad (2)$$

where $\boldsymbol{S} = \boldsymbol{S}_1 + \boldsymbol{S}_2$ ($S = 0, 1, 2$) and $\boldsymbol{D}_S$ is the dimer's anisotropy for a given state with total spin S. The energy levels are readily obtained in the purely axial anisotropy limit:

$$E = -JS(S+1) + D_S[M_S^2 - S(S+1)/3] \qquad (3)$$

D_S can be expressed as a function of D_0 (defined for convenience as $3D_0 = D_1 = D_2$) for each $S \geq 1$ level: $D_{S=1} = -3D_0$ and $D_{S=2} = +D_0$. Interestingly, the ZFS parameters for the $S = 1$ and $S = 2$ cluster states are opposite in sign.

The magnetic susceptibility shown in Fig. 4 was fitted[23] using this model. Two sets of parameters were found to account for the susceptibility data: (a) $J = +0.31$ meV, $D_0 = -0.08$ meV, $g = 2.22$ and (b) $J = +0.33$ meV, $D_0 = +0.09$ meV, $g = 2.23$. An isotropic model ($D_0 = 0$) failed to explain the low temperature downturn. On the other hand, as anticipated, magnetic susceptibility on powder samples alone cannot reliably predict the sign of the single-ion anisotropy. In the basis $|S, M_S\rangle$, the lowest level in the $S = 2$ ground state is therefore either (a) $|2,2\rangle$ or (b) $|2,0\rangle$. The energy diagram for each solution is schematically represented in Fig. 10.
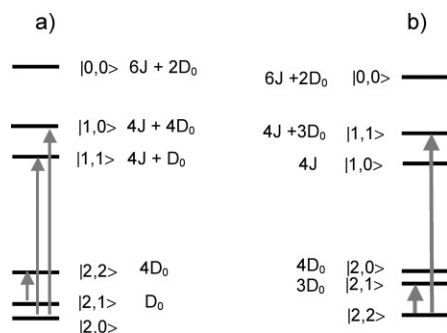

Fig. 10 Energy levels in the $|S, M_S\rangle$ basis diagram for **1** in the negative and positive D_0 case as discussed in the text. (a) $D_0 = 0.08$ meV, $J = 0.33$ meV (b) $D_0 = -0.09$ meV, $J = 0.32$ meV. Solid arrows on the right-hand side graph represent the observed INS transitions at 0.27 meV and 1.57 meV. Solid arrows on the left-hand side represent the INS transitions expected in the $D_0 > 0$ case.

To determine whether D_0 is negative or positive we now consider the INS results. Only one single peak at $\hbar\omega_1 = 1.57$ meV has been observed in the energy window between 0.5 and 2.2 meV. A weak and unresolved peak is also observed around $\hbar\omega_2 = 0.27$ meV. Both cases, D_0 negative or positive, have been considered to analyse the INS data. The expected INS transitions in each case are shown as arrows in Fig. 10. If D_0 is positive, one transition at very low energy (0.08 meV) and two transitions between 1.4 and 1.7 meV are expected. The first one would be too low in energy and therefore out of our reach but the last two transitions together could account for the $\hbar\omega_1 = 1.57$ meV peak, assuming unresolved peaks. If D_0 is negative, two transitions are possible. The first one at $\hbar\omega = 3D_0$ is close to the observed peak $\hbar\omega_2 = 0.27$ meV while the second one at $\hbar\omega = 4J + 3D_0$ would then correspond to the higher energy peak $\hbar\omega_1 = 1.57$ meV peak. This is clearly confirmed by comparing the INS spectra at 1.5 K and 5 K (see Fig.-5) with simulated spectra using $J = 0.32$ meV and either $D_0 = +0.09$ meV (dashed line) or $D_0 = -0.09$ meV (solid line). Therefore, our INS data strongly favour a negative single-ion anisotropy D_0.

From the INS data we obtain $3D_0 = 0.27$ meV and $4J + 3D_0 = 1.57$ meV and we can deduce the exchange coupling and anisotropy parameters: $J = 0.32$ meV and $D_0 = -0.09$ meV. They differ slightly from the values obtained from the susceptibility. This discrepancy is perfectly accounted for by having a slightly different g-factor ($g = 2.23$ instead of 2.22). A calculated χT curve using these values is represented in Fig. 4 (solid line). To underline the effect of

anisotropy, χT in the isotropic limit (D_0) and the same g-factor and exchange interaction is shown as well (dashed line).

We have thus conclusively determined the microscopic magnetic parameters of **1** using magnetic susceptibility and INS measurements. The ZFS parameter in the $S = 2$ ground state is given by $D_{S=2} = +D_0 = -0.09$ meV ≈ -1.0 K and **1** is expected to be a single molecule magnet with an extremely small energy barrier, $\Delta = |D_{S=2}|S^2 \approx 4.26$ K.

[Ni$_4$(μ_3-OMe)$_4$(O$_2$CCMe$_3$)$_4$(MeOH)$_4$] 4.5 MeOH 2

According to the cubane-like geometry of the cluster (see Figs. 2 and 6), the appropriate effective exchange Hamiltonian is given by:

$$H_{Ni4cub} = -2J(\boldsymbol{S}_1 \cdot \boldsymbol{S}_2 + \boldsymbol{S}_3 \cdot \boldsymbol{S}_4) - 2J'(\boldsymbol{S}_1 + \boldsymbol{S}_2) \cdot (\boldsymbol{S}_3 + \boldsymbol{S}_4) \qquad (4)$$

Using the Kambe coupling scheme, the Hamiltonian becomes:

$$H_{Ni4cub} = (J' - J)(\boldsymbol{S}_{12}^2 + \boldsymbol{S}_{34}^2) - J'\boldsymbol{S}_T^2 \qquad (5)$$

with $\boldsymbol{S}_{12} = \boldsymbol{S}_1 + \boldsymbol{S}_2$, $\boldsymbol{S}_{34} = \boldsymbol{S}_3 + \boldsymbol{S}_4$ and $\boldsymbol{S}_T = \boldsymbol{S}_{12} + \boldsymbol{S}_{34}$. Here, J and J' are the exchange parameters defined in Fig. 6.

All couplings are bridged by two μ_3-methoxides, however the Ni–Ni distances are significantly different [Ni(1)–Ni(2) = 2.85 Å and Ni(1)–Ni(3) = 3.14 Å] which justifies two different exchange couplings. The susceptibility data (Fig. 6) clearly shows that FM couplings are dominant. The χT product at low temperatures is compatible with $S = 4$ in the ground state. We therefore assume, in a first approximation, that both J and J' are ferromagnetic in nature (see later). The energy levels are then given by:

$$E = (J' - J)[S_{12}(S_{12}+1) + S_{34}(S_{34}+1)] - J'S_T(S_T+1) \qquad (6)$$

where $0 < S_{12} < 2$, $0 < S_{34} < 2$, $|S_{12} - S_{34}| < S_T < S_{12} + S_{34}$.

For FM (> 0) J and J', the ground state is necessarily $S = 4$ irrespective of the relative strength of J and J' and there are two $S = 3$ states at energies given by: $\hbar\omega_1 = 8J'$ and $\hbar\omega_2 = 4J + 4J'$. Since the INS selection rules allow only transitions between spin states with $\Delta S = S - S' = 0$ and ± 1, it is reasonable to assume that the two observed peaks (Fig. 7) are transitions from the $S = 4$ ground state to the $S = 3$ states. We can then calculate J and J' using eqn. (6). Two sets of parameters are found: (a) $J = 1.08$ meV, $J' = 0.59$ meV and (b) $J = 0.35$ meV, $J' = 0.83$ meV depending on whether $\hbar\omega_1 = 8J'$ or $\hbar\omega_2 = 4J + 4J'$ lies lowest, respectively. Both the susceptibility (Fig. 6) and the INS data (Fig. 7) have been analysed using these two sets of parameters, and we find that only model a) is compatible with the susceptibility *and* the INS data. However, single-ion anisotropy has to be included to account for the low temperature downturn in χT (see Fig. 6). A best agreement with both the χT curve and the neutron data is found with $J = 1.04$ meV, $J' = 0.56$ meV, $g \approx 2.0$. As in the dimer case (see eqn. (1)), the effect of anisotropy can be qualitatively estimated by considering only an axial single-ion anisotropy contribution, taken to be identical for all four Ni(II) sites, which can be either positive ($D_{i=1,2,3,4} = 0.38$ meV) or negative ($D_i = -0.27$ meV). This is only an approximate estimate since the cluster does not have a purely axial symmetry (see Fig. 2).

Fig. 11 shows the calculated energy levels for the $S = 4$ and $S = 3$ states, for these two situations along with the isotropic case ($D_i = 0$). One can see that ZFS is significant only for the $S = 4$ state. The absolute values of D_i are close to those obtained in **1** but, from the present data, we cannot reliably decide between these two solutions. Further studies (low temperature AC susceptibility or high frequency EPR spectroscopy for instance) are required to determine the sign of D_i. Note that the cluster anisotropy in the $S = 4$ ground state, $D_{S=4}$, is related to D_i by: $D_{S=4} = (1/7)D_i$. In the case where $D_i < 0$ we would then have $D_{S=4} = -0.035$ meV $= -0.40$ K and therefore the system would have an energy barrier in the ground state of about $\Delta = |D_{S=4}|S^2 = 6.4$K. Recent results[24] from Hendrickson and co-workers on a similar nickel cubane suggest that the negative D-value is more likely.
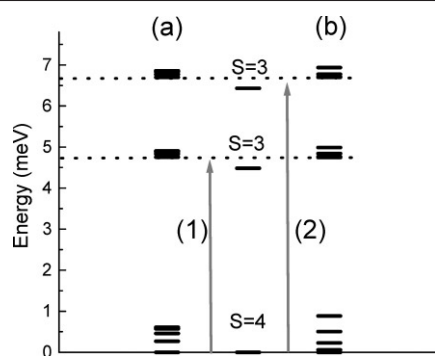
Fig. 11 Energy level diagram for **2** as determined from INS and susceptibility measurements. From left to right are represented the $S = 4$ and $S = 3$ levels for $D_i = -0.27$ meV (left), $D_i = 0$ (middle), $D_i = +0.38$ meV (right). The exchange parameters are $J = 1.04$ meV and $J' = 0.56$ meV. The observed INS transitions at (1) 4.75 meV and (2) 6.7 meV are shown as solid arrows.

[Ni$_4$(μ_3-OH)$_2$(O$_2$CCMe$_3$)$_6$(EtOH)$_6$]. 2EtOH 3

Magnetic exchange pathways in **3** are schematically shown in Fig. 8. This is the well-known "butterfly"-type of arrangement with a centre of inversion C_i. Considering Ni–Ni distances and Ni–O–Ni angles, three different exchange couplings should be relevant: J_0 is the "core" coupling between the two central ions and is mediated by two μ_3-oxo bridges; J_1 and J_2 are the "wing" couplings and are primarily made up of one μ_3-oxo bridge. It is worth noting that the Ni–Ni distances and bond angles are quite different in this structure: Ni(1)–Ni(2) = 3.09 Å, Ni(1)–Ni(3) = Ni(2)–Ni(4) = 3.32 Å, Ni(1)–Ni(4) = Ni(2)–Ni(3) = 3.69 Å and 97° < Ni–O–Ni < 128°. Consequently, we expect significant differences in the coupling strength. Based on these structural information, the appropriate effective spin Hamiltonian is given by:

$$H_{\text{Ni4but}} = -2J_0\boldsymbol{S}_1\cdot\boldsymbol{S}_2 - 2J_1(\boldsymbol{S}_1\cdot\boldsymbol{S}_3 + \boldsymbol{S}_2\cdot\boldsymbol{S}_4) - 2J_2(\boldsymbol{S}_1\cdot\boldsymbol{S}_4 + \boldsymbol{S}_2\cdot\boldsymbol{S}_3) \quad (7)$$

where J_0 is the core exchange coupling. J_1 and J_2 are the short and long wingtip exchange couplings, respectively. The Kambe coupling scheme cannot be applied if $J_1 \neq J_2$. Then the energy levels have to be evaluated numerically.

The susceptibility data (Fig. 8) clearly shows that the χT product goes to zero at low temperature. This is strongly indicative of an $S = 0$ ground state and therefore dominant AFM interactions in this compound. A simple model using the three exchange couplings defined above leads to the following conclusions: Having $J_1 = J_2 < 0$ and $J_0 < 0$ or $J_0 > 0$ does not lead to a satisfactory result. A good fit to the data is obtained with $J_1 = -1.7$ meV, $J_2 = -0.20$ meV, $J_0 = +0.20$ meV and $g = 2.19$ as shown in Fig. 12. The situation here is much closer to two weakly coupled AFM dimers, Ni(1)–Ni(3) and Ni(2)–Ni(4), than to that of a genuine butterfly geometry, where J_0 is usually assumed to be the strongest coupling. However, one should consider this set of parameters as indicative, only the main picture should be considered firm and solid, due to the large number of adjustable parameters.

To assess the relevance of the above set of parameters, a simulation using these parameters in eqn. (7) is compared to the INS spectrum in Fig. 9: the result is shown as a thin solid line. With the above parameters, the energy level scheme is straightforward. Above the $S = 0$ ground state there are two $S = 1$ levels in the energy range spanned by our INS study and only two allowed transitions.

As shown (Fig. 9) the lower energy peak at $\hbar\omega_1 = 2.86$ meV is well accounted for by the model but the higher energy peaks are not, with the exception of the peak around $\hbar\omega_3 = 4.50$ meV. No better agreement could be found using just an isotropic model. One possibility to improve the quality of the agreement is to introduce single-ion anisotropy. In this case the $S = 1$ levels split and the two peaks obtained in the isotropic model are now split in two as represented in Fig. 13. The best agreement to the INS data is shown in Fig. 9 (thick solid line) with the exchange parameters $J_1 = -1.9$ meV, $J_2 = +0.2$ meV, $J_0 = -0.2$ meV and a single-ion
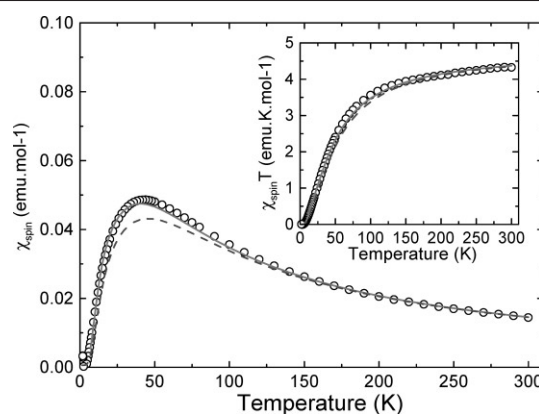

Fig. 12 DC-SQUID spin susceptibility χ_{spin} (solid circles) of **3** between 1.5 K and 300 K under an applied external field of 1000G. The inset shows χ represented as χT *versus* T. The solid line represents a best fit[23] to the data as discussed in the text using an isotropic model with three exchange couplings ($J_0 = 0.20$ meV, $J_1 = -1.7$ meV, $J_2 = -0.20$ meV and $g = 2.19$) while the dashed line is a calculation based on conclusions derived from the INS spectrum ($J_0 = -0.2$ meV, $J_1 = -1.9$ meV, $J_2 = +0.2$ meV, $D_i = 1.0$ meV and $g = 2.19$).
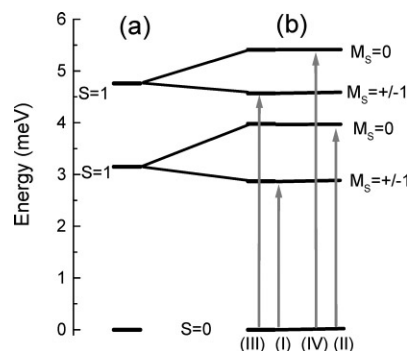

Fig. 13 Energy level diagram for **3** as determined from INS and susceptibility measurements. (a) isotropic case ($D_i = 0$) with $J_0 = -0.2$ meV, $J_1 = -1.9$ meV and $J_2 = +0.2$ meV. (b) anisotropic case ($D_i = +1.0$ meV) with the same J values as in (a). Only the $S = 0$ ground state and first two $S = 1$ levels have been represented. Solid arrows on the right-hand side represent the observed INS transitions at 2.87, 3.98, 4.56 and 5.41 meV as also shown in Fig. 9.

anisotropy term $D_i = +1.0$ meV identical for all four Ni(II) ions. This last assumption is qualitatively justified by the almost parallel orientation of the NiO$_6$ octahedra. Assuming negative single-ion anisotropy does not lead to a good reproduction of the INS data.

Compared to the isotropic model, the overall agreement is improved. There are four peaks, located at 2.87, 3.98, 4.56 and 5.41 meV, corresponding to the INS transitions shown in Fig. 13. Transitions (I)–(III) are relatively well accounted for within a few percent except for the intensity of transition (III) where a 30% mismatch is found. On the other hand, transition (IV) is only loosely accounted for both in terms of energy position and intensity. There is a 4% mismatch in the energy position and a factor 3 in the intensity. Swapping the sign of J_0 and J_2 did not improved the agreement. We find that the susceptibility is well reproduced using this set of parameters (dashed line in Fig. 12) even if the agreement is slightly poorer than that with the isotropic model (solid line in Fig. 12). The necessity to include a very large single-ion anisotropy is quite striking but it is important to stress that due to the ground state being $S = 0$, the susceptibility is only marginally affected by inclusion of single-ion anisotropy. However, the fit of the INS spectrum is improved. The energy level pattern, restricted to the first two $S = 1$ levels is shown in Fig. 13 using the above parameters. Finally we would like to comment the overall quality of the modelling. Several shortcomings in the model could explain the mismatch between the experimental data and the modelling. We find that having different D_i for the two inequivalent Ni(II) sites (core and wing ions) does not improve the results and only add one more adjustable parameter. However a more complicated set of anisotropy tensors, including

significant higher order terms could account for the mismatch. In short, while the present data do not contain enough information to unambiguously determine all the exchange couplings *and* all the single-ion anisotropy terms, we have shown that INS can indeed provide crucial bits of information that are not accessible from bulk magnetometry measurements.

Conclusions

For the three compounds under investigation we have derived the exchange couplings between Ni(II) ions. In all cases, the coupling is mediated principally by μ-oxygen bridges and one can draw some correlations between the coupling strength and the Ni–O–Ni angles defined by the μ-oxygen bridge. As has been shown previously,[16,25] there is a clear trend with ferromagnetic coupling observed for small Ni–O–Ni angles and AFM couplings at higher angles.

The combination of inelastic neutron scattering and magnetic susceptibility measurements permits an unambiguous assignment of the exchange couplings, and this allows a better estimate of the zero-field splitting than could be obtained if we had only fit the variable temperature susceptibility. Unfortunately pivalate is a far from ideal ligand for neutron scattering, and therefore the data is not ideal. Therefore while for **1** the ground state *D*-value is well determined and for **3** the *D*-value in the excited state can be calculated, for **2** two possible values for the *D*-value are found. The ideal method for measuring this value is high frequency EPR spectroscopy, and experiments to measure spectra of **2** at 95 GHz are proceeding and will be reported later.

The three nickel complexes reported here are equivalent to cobalt(II) pivalate cages discussed previously.[26] The cobalt chemistry was found to be extremely complicated due to the ready oxidation of Co(II) to Co(III). This problem is not encountered with the nickel compounds, however **1** is a very useful starting material for making other nickel cage complexes, and heterometallic cage compounds.[27]

Acknowledgements

References

1 (*a*) R. Sessoli, H.-L. Tsai, A. R. Schake, S. Wang, J. B. Vincent, K. Folting, D. Gatteschi, G. Christou and D. N. Hendrickson, *J. Am. Chem. Soc.*, 1993, **115**, 1804; (*b*) R. Sessoli, D. Gatteschi, A. Caneschi and M. A. Novak, *Nature*, 1993, **365**, 141.

2 D. Gatteschi and R. Sessoli, *Angew. Chem., Int. Ed. Engl.*, 2003, **42**, 268.

3 M. N. Leuenberger and D. Loss, *Nature*, 2001, **410**, 789.

4 (*a*) I. Mirebeau, M. Hennion, H. Casalta, H. Andres, H.-U. Güdel, A. V. Irodova and A. Caneschi, *Phys. Rev. Lett.*, 1999, **83**, 628; (*b*) R. Caciuffo, G. Amoretti, A. Murani, R. Sessoli, A. Caneschi and D. Gatteschi, *Phys. Rev. Lett.*, 1998, **81**, 4744; (*c*) H. Andres, R. Basler, H.-U. Güdel, G. Aromi, G. Christou, H. Büttner and B. Rufflé, *J. Am. Chem. Soc.*, 2000, **122**, 12469; (*d*) J. M. Clemente, M. Aebersold, J. J. Borras-Almenar, E. Coronado, H. U. Güdel, D. Kearley and H. Büttner, *J. Am. Chem. Soc.*, 1999, **121**, 10021; (*e*) H. Andres, J. M. Clemente, M. Aebersold, E. Coronado, H. U. Güdel, D. Kearley and H. Büttner, *J. Am. Chem. Soc.*, 1999, **121**, 10028.

5 J. Cosier and A. M. Glazer, *J. Appl. Crystallogr.*, 1986, **19**, 105–7.

6 P. T. Beurskens, G. Beurskens, W. P. Bosman, R. de Gelder, S. Garcia-Granda, R. O. Gould, R. Israel, J. M. M. Smits, *DIRDIF-96*, program system, University Crystallography Laboratory, University of Nijmegen 1996.

7 G. M. Sheldrick, *SHELXS-97, Program for solution of crystal structures*, University of Göttingen, Germany, 1997; G. M. Sheldrick, *SHELXL-97, Program for refinement of crystal structures*, University of Göttingen, Germany, 1997.

8 (*a*) U. Turpeinen, *Finn. Chem. Lett.*, 1976, 173; (*b*) U. Turpeinen, *Finn. Chem. Lett.*, 1977, 36; (*c*) U. Turpeinen, *Finn. Chem. Lett.*, 1977, 123; (*d*) U. Turpeinen, M. Ahlgren and R. Hamalainen, *Finn. Chem. Lett.*, 1977, 246; (*e*) M. Ahlgren, R. Hamalainen and U. Turpeinen, *Cryst. Struct. Commun.*, 1977, 829; (*f*) M. Ahlgren, R. Hamalainen and U. Turpeinen, *Acta Chem. Scand. A.*, 1978, **32**, 189; (*g*) M. Ahlgren and U. Turpeinen, *Acta Crystallogr., Sect. B.*, 1982, **B38**, 276.

9 C. L. H. Kennard, E. J. O'Reilly and G. Smith, *Polyhedron*, 1984, **3**, 689.

10 B.- H. Ye, I. D. Williams and X.- Y. Li, *J. Inorg. Biochem.*, 2002, **92**, 128.

11 P. Chaudhuri, H.-J. Kuppers, K. Wieghardt, S. Gehring, W. Haase, B. Huber and J. Weiss, *J. Chem. Soc., Dalton Trans.*, 1988, 1367.

12 L. Eremenko, S. E. Nefedov, A. A. Sidorov, M. A. Golubnichaya, P. V. Danilov, V. N. Ikorskii, Yu. G. Shvedenkov, V. M. Novotortsev and I. I. Moiseevm, *Inorg. Chem.*, 1999, **38**, 3764.

13 (*a*) I. L. Eremenko, M. A. Golubnichaya, S. E. Nefedov, A. A. Sidorov, I. F. Golovaneva, V. I. Burkov, O. G. Ellert, V. M. Novotortsev, L. T. Eremenko, A. Sousa and M. R. Bermejo, *Russ. Chem. Bull.*, 1998, 725; (*b*) A. A. Sidorov, M. O. Ponina, S. M. Deomidov, V. M. Novotortsev, A. Demonceau, S. E. Nefedov, I. L. Eremenko and I. I. Moiseev, *Chem. Commun.*, 2000, 1383.

14 J. E. Andrew and A. B. Blake, *J. Chem. Soc. A*, 1969, 1456.

15 V. G. Kessler, S. Gohil, M. Kritikos, O. N. Korsak, E. E. Knyazeva, I. F. Moskovskaya and B. V. Romanosky, *Polyhedron*, 2001, **20**, 915.

16 M. A. Halcrow, J.-S. Sun, J. C. Huffman and G. Christou, *Inorg. Chem.*, 1995, **34**, 4167.

17 M. S. El Fallah, E. Rentschler, A. Caneschi and D. Gatteschi, *Inorg. Chim. Acta*, 1996, **247**, 231.

18 M. Darensbourg, R. M. Buonomo and J. H. Reibenspies, *Z. Kristallogr.*, 1995, **210**, 469.

19 A. J. Blake, E. K. Brechin, A. Codron, R. O. Gould, C. M. Grant, S. Parsons, J. M. Rawson and R. E. P. Winpenny, *J. Chem. Soc., Chem. Commun.*, 1995, 1983.

20 A. A. Sidorov, I. G. Fomina, S. S. Talismanov, G. G. Aleksandrov, V. M. Novotortsev, S. E. Nefedov and I. L. Eremenko, *Koord. Khim.*, 2001, **27**, 584.

21 V. V. Pavlishchuk, S. V. Kolotilov, A. W. Addison, M. J. Prushan, D. Schollmeyer, L. K. Thompson, T. Weyhermuller and E. A. Goreshnik, *Dalton Trans.*, 2003, 1587.

22 R. L. Carlin, *Magnetochemistry*, Springer-Verlag, Berlin, 1986, p. 63.

23 The experimental data was fit using the Levenberg–Marquardt least-squares fitting algorithm, in combination with MAGPACK. References to MAGPACK can be found in:(*a*) J. J. Borrás–Almenar, J. M. Clemente–Juan, E. Coronado and B. S. Tsukerblatt, *Inorg. Chem.*, 1999, **38**, 6081; J. J. Borras-Allmenar, J. J. Clemente, E. Coronado and B. Tsukerblat, *J. Comput. Chem.*, 2001, **22**, 985.

24 E.-C. Yang, W. Wernsdorfer, S. Hill, R. S. Edwards, M. Nakano, S. Maccagnano, L. N. Zakharov, Lev, A. L. Rheingold, G. Christou and D. N. Hendrickson, *Polyhedron*, 2003, **22**, 1727–1733.

25 K. K. Nanda, L. K. Thompson, J. N. Bridson and K. Nag, *J. Chem. Soc., Chem. Commun.*, 1994, 1337.

26 G. Aromi, A. S. Batsanov, P. Christian, M. Helliwell, A. Parkin, S. Parsons, A. A. Smith, G. A. Timco and R. E. P. Winpenny, *Chem. Eur. J.*, 2003, **9**, 5142.

27 (*a*) G. Aromí, A. S. Batsanov, P. Christian, M. Helliwell, O. Roubeau, G. A. Timco and R. E. P. Winpenny, *Dalton Trans.*, 2003, 4466; (*b*) F. K. Larsen, E. J. L. McInnes, H. El Mkami, J. Overgaard, S. Piligkos, G. Rajaraman, E. Rentschler, A. A. Smith, G. M. Smith, V. Boote, M. Jennings, G. A. Timco and R. E. P. Winpenny, *Angew. Chem., Int. Ed. Engl.*, 2003, **42**, 101.